Development of Tannin-bridged Cerium Oxide Microcubes-chitosan Cryogel as a Multifunctional Wound Dressing

Muzhou Teng
Southern Medical University
Zhijia Li
Southern Medical University
Zhihui Lu
Southern Medical University
Keke Wu
Southern Medical University
Jinshan Guo (jsguo4127@smu.edu.cn)
Southern Medical University https://orcid.org/0000-0001-8097-4902

Research

Keywords: Tannic acid, CeO2, Chitosan, Hydrogen bonding, Cryogel, Wound healing

Posted Date: November 17th, 2021

DOI: https://doi.org/10.21203/rs.3.rs-1043996/v1

Version of Record: A version of this preprint was published at Colloids and Surfaces B: Biointerfaces on March 1st, 2022. See the published version at https://doi.org/10.1016/j.colsurfb.2022.112479.

Abstract

Background: Efficient resolution of oxidative stress, inflammation and bacterial infections are crucial for wound healing. To surmount these problems, tannic acid (TA)-bridged CeO_2 microcubes and chitosan (CS) (CS-TA@CeO_2) cryogel was fabricated through hydrogen bonding interactions as a multifunctional wound dressing.

Results: The physicochemical characterizations confirmed the successful introduction and uniform incorporation of TA@CeO_2 microcubes into CS network. Thus-obtained CS-TA@CeO_2 cryogels displayed suitable porous structure and swelling ratio. The CS-TA@CeO_2 cryogels exhibited favorable antioxidant ability evidenced by scavenging more than 82.9% ROS *in vitro* and significantly increasing the antioxidant enzyme levels *in vivo*. The anti-inflammatory ability of the cryogels was confirmed by the downregulated expression of the inflammatory cytokine, tumor necrosis factor-alpha (TNF-α) and the upregulated expression of the anti-inflammatory cytokine, interleukin-10 (IL-10). The multifunctional cryogels also showed excellent antibacterial activities against Gram-positive (*S.aureus*) and Gram-negative (*E.coli*) bacteria. Furthermore, the cryogels can promote the adhesion and proliferation of mouse fibroblasts (L929) cells. Moreover, CS-TA@CeO_2 cryogels presented excellent hemostatic performance in rat tail amputation model. *In vivo* Sprague-Dawley (SD) rats full-thickness experiments illustrated that the cryogels can significantly accelerate wound healing through providing considerable antioxidant activity, promoting angiogenesis, and increasing collagen deposition.

Conclusions: Overall, the multifunctional CS-TA@CeO_2 cryogels showed great potential for wound healing.

Background

Skin injury, caused by burns, surgery, trauma or chronic disease (such as diabetes), has become one of the most critical clinical issues [1, 2]. Generally, the healing of wounded skin is a complex process including four continuous and overlapping phases: hemostasis, inflammation, proliferation and remodeling [3]. Although inflammation is an essential wound healing phase, abnormally and persistent inflammation may cause the release of inflammatory cytokines and the elevation of reactive oxygen species (ROS) level, leading to uncontrolled tissue damage and delayed wound healing [4]. Meanwhile, it has been documented that excessive ROS production can induce oxidative stress and strong inflammatory response, which makes wounds vulnerable and postpones wound healing process [5]. Besides, accumulated excessive ROS in the wound site can severely affect angiogenesis and lead to endothelial dysfunction [6]. Thus, the development of multifunctional wound dressings with antioxidant, anti-inflammatory, antibacterial, rapid hemostatic, and angiogenetic properties, which can modulate wound inflammation microenvironment by scavenging excessive ROS and reducing inflammatory factors, is urgently needed [7, 8].

Chitosan (CS), a polysaccharide derived from naturally abundant chitin, with favorable biocompatibility, antibacterial activity and effective hemostatic performance, has received intensive attention in biomedical research area, especially as wound dressing material [9–12]. Recently, compositing CS with nanoparticles, such as copper (Cu), zinc oxide (ZnO) and titanium dioxide (TiO_2) nanoparticles, has become an effective strategy for fabricating novel CS-based wound dressings with superior wound healing ability [13, 14]. Ceria (cerium oxide, CeO_2) nanoparticles have demonstrated efficient ROS scavenge and cell protecting ability against oxidative stress due to the reversible transition between the reduced (Ce^{3+}) and oxidized (Ce^{4+}) states of cerium ions on the particle surface [15, 16]. Recently, it has been reported that CeO_2 nanoparticles could accelerate wound healing by promoting cell proliferation and vascularization [17]. However, pure CeO_2 nanoparticles have a dose toxicity, that is to say, high concentrations of CeO_2 nanoparticles would bring cytotoxicity [18, 19]. Besides, the fast release of CeO_2 nanoparticles may cause severe nanotoxicity. Excitingly, immobilizing inorganic particles into organic polymer networks has been proved a possible strategy to address the nanotoxicity issue [20–23]. Tannic acid (TA), a natural polyphenol composing of a central glucose and 10 galloyl ester groups in total, has already been approved by the FDA for applications in food and medicine area [24, 25]. It is reported that TA can interact with various polymers, such as polyvinyl alcohol (PVA) [26], polypoly(ethylene glycol) (PEG) [27], gelatin [28], and so on, through hydrogen bonding. Thus the surface modification of CeO_2 nano-/micro-particles with TA can confer them hydrogen-bonding sites to interact with organic polymers [29, 30], which could immobilize CeO_2 nano-/micro-particles in the polymer network to slow down the release of the particles and reduce their toxicity. Moreover, TA can render intrinsic anti-inflammatory and antioxidant properties to the biomaterials [26, 27]. Besides, the application of antibacterial TA in wound dressing might eliminate antibiotic treatment for wound healing, avoiding severe cytotoxicity and drug resistance [28, 29]. Moreover, TA can interact with blood-borne proteins, demonstrating excellent hemostatic property [31].

Cryogels, prepared via freezing/low temperature cryogelation process, possess highly interconnected and porous structure, thus can absorb the excessive wound exudate and provide a moist environment for wound healing. Moreover, cryogels also can provide an environment similar to the extracellular matrix (ECM) of native tissues, which is conducive to cell migration and oxygen permeabilization to accelerate wound healing [32, 33]. Herein, TA-bridged CeO_2 microcubes and CS (CS-TA@CeO_2) cryogels were fabricated as a multifunctional wound dressing (Scheme 1). The physicochemical composition and structure of the CS-TA@CeO_2 cryogels were characterized, and the biocompatibility, cell proliferation, antibacterial, antioxidant and angiogenic performance, as well as wound closure efficacy of the crogels were investigated both *in vitro* and *in vivo*. The obtained multifunctional cryogels exhibited excellent hemostatic, anti-inflammatory, antibacterial, antioxidant and angiogenic properties, as well as good biocompatibility, thus could effectively promote wound healing.

Results And Discussion

Characterizations of CS-TA@CeO_2 cryogels

The chemical structures of CS-TA@CeO_2 cryogels were investigated by FTIR analysis, the results were shown in Figures 1A and 1B. As can be seen, pure TA showed characteristic peaks of C=O (stretching vibration, 1714 cm^{-1}) and phenolic hydroxyl groups on the benzene rings (3000-3500 cm^{-1}) [34, 35]. Compared to pure CeO_2 microcubes, it can be seen that TA@CeO_2 microcubes displayed characteristic peaks of TA at 1714 and 1194 cm^{-1}, indicating that TA adhesive layer was successfully adhered on the surface of CeO_2 microcubes. As shown in Figure 1B, CS showed characteristic absorption bands at 2878, 1590, 1416 and 1075 cm^{-1}, which assigned to stretching vibration of C-H, bending of N-H, bending of C-H and stretching of C-O bonds, respectively [36]. With the addition of TA@CeO_2 microcubes, the characteristic peak at 3000-3500 cm^{-1} enhanced, indicating TA@CeO_2 microcubes successfully anchored in CS network.

The X-ray diffractometer (XRD) spectra of CeO_2, CS and CS-TA@CeO_2 cryogels are presented in Figure 1B. It can be seen that the diffraction peaks of CeO_2 appeared at 2θ of 28.59, 33.15, 47.64, 56.51, 59.23, 69.49, and 76.77°, which were assigned to the Miller indices (111), (200), (220), (311), (222), (400), (331), (420), and (422), respectively, matching with the cubic phase of CeO_2 (JCPDS #89-8436) [15, 17]. For CS, a broad peak at 2θ = 20.37° showed up, which was attributed to the amorphous state of chitosan [37]. In the XPS spectra of CS-TA@CeO_2 cryogels, with the increase of CeO_2 content, the characteristic peaks of CeO_2 also gradually enhanced.

The thermal properties of CS-TA@CeO_2 cryogels were investigated by thermogravimetry analysis (TGA). From the TGA curves shown in Figure 1C, two weight loss stages can be seen. The first weight loss stage was around 100 °C, which was considered to be the release of the trapped water. The second significant weight loss stage was from 220 °C to 320 °C, which was attributed to the decomposition of CS polymer chain [37].

Morphology, porosity and swelling ratio evaluation of CeO_2 and CS-TA@CeO_2 cryogels

The morphologies of CeO_2, TA@CeO_2 and CS-TA@CeO_2 cryogels observed by SEM are shown in Figures 2A-J. It can be seen that both CeO_2 and TA@CeO_2 nanoparticles were uniformly dispersed without any aggregation, displaying a cubic structure with a length about 2.5 μm (Figures 2A and 1B). From Figures 2C-F, it can be seen that CS and CS-TA@CeO_2 cryogels displayed interconnected porous structures with a pore diameter of 15-30 μm. After the doping of TA@CeO_2, the porous structure was kept for CS-TA@CeO_2 cryogels (Figures 2G-J). The quantitative porosity ratios were further determined by an alcohol immersion method. As shown in Figure 2K, the porosity of CS cryogels was 92.32%, while that of CS-TA@CeO_2-5%, CS-TA@CeO_2-10% and CS-TA@CeO_2-15% cryogels were 86.15%, 84.34% and 80.16%, respectively. The

decrease of porosities might be caused by the gravity of the loaded CeO_2, which suppressed the pore cavities. The pores of CS-TA@CeO_2 cryogel also became more flat comparing to that of CS cryogel. The relatively high porosity of CS-TA@CeO_2 cryogels is desirable for cell penetration, as well as hemostasis, oxygen exchange and exudate absorption, beneficial for wound healing [38, 39]. Furthermore, with the content of TA@CeO_2 increasing, more particles could be observed in the cryogels, indicating the successful incorporation of TA@CeO_2 in CS networks.

Swelling is an essential property of cryogels, enabled the cryogels to absorb excessive exudate of the wound, and provide a moist environment beneficial to wound healing [40-42]. Also, the porous structure is conducive to cell migration and provides excellent oxygen permeability, which could accelerate wound healing [43, 44]. Therefore, the swelling ratios of cryogels were evaluated, and the results are shown in Figure 2L. It can be seen that all of the CS and CS-TA@CeO_2 cryogels exhibited swelling ratios all higher than 1400 wt%, which was attributed to the interconnected network and microporous structure of the cryogels. Interestingly, with the addition of TA@CeO_2, the swelling ratios of the cryogels decreased. The swelling ratio of CS was 1751.64 wt%, and the swelling ratios of CS-TA@CeO_2 with 5, 10, and 15 wt% TA@CeO_2 were 1430.80, 1436.02 and 1502.56 wt% respectively, which might be caused by the crosslinking effect raised by the intermolecular hydrogen bonding between CS and TA@CeO_2 [3, 40].

Antioxidant activity of CS-TA@CeO_2 cryogels *in vitro* and *in vivo*

ROS played a critical role in inflammation during wound healing, but overdose ROS would result in oxidative stress, leading to cell and tissue damage [5, 45]. Herein, the antioxidant activities of pure CS and CS-TA@CeO_2 cryogels were evaluated by testing the scavenging efficiency of DPPH free radicals. As shown in Figures 3A and 3B, CS-TA@CeO_2 cryogels could obviously decrease the absorption peak intensity of DPPH free radicals, and the scavenge percentages were 35.63% (CS-TA@CeO_2-5%), 59.69% (CS-TA@CeO_2-10%), and 82.90% (CS-TA@CeO_2-15%), respectively. However, CS displayed almost no DPPH free radical scavenge ability with only 1.72% radical scavenge. With the increasing of CeO_2 content, the absorption peak intensity of DPPH free radicals decreased significantly, indicating that the excellent antioxidant activity of CS-TA@CeO_2 cryogels was endowed by CeO_2.

Furthermore, the *in vivo* anti-oxidative activity was also evaluated. ROS is eliminated by the complex antioxidant defense systems *in vivo*, such as superoxide dismutase (SOD) and catalase (CAT), which are considered as the most important antioxidant enzymes. Thus, increasing the expression levels of SOD and CAT can reduce oxidative stress and promote wound healing [35]. As shown in Figures 3C and 3D, for all groups, the SOD and CAT activities increased with healing time until the 14^{th} day, but decreased at the 21^{nd} day. Moreover, the groups treated with CS-TA@CeO_2-15% cryogels showed a remarkable higher SOD

and CAT activities comparing to other groups at day 7 and 14. These results further confirmed the anti-oxidative ability of CS-TA@CeO_2 cryogels by mitigating oxidative stress at the wound sites *in vivo*.

Antibacterial activity of CS-TA@CeO_2 cryogels

Bacterial infection has remained a challenging issue, which delays the healing process. Thus, wound dressings with antibacterial ability have a great potential in clinical applications [46-48]. The antibacterial activity of CS-TA@CeO_2 cryogels was evaluated by measuring the diameter of bacterial inhibition zone first [49]. As shown in Figures 4A and 4B, no inhibition zone was observed for pure CS cryogels (a), while the average diameter of the inhibition zone was around 12.2 mm and 13.1 mm against *S. Aureus*, and around 11.5 mm and 12.5 mm against *E. Coli*, for CS-TA@CeO_2-10% (b) and CS-TA@CeO_2-15% (c) cryogels respectively. Besides, the continuous inhibitory effect of CS-TA@CeO_2 cryogels on the bacterial growth curve was also investigated and the results are shown in Figure 4C. It can be found that the growth profiles of both bacteria were significantly hampered, and the inhibitory effect enhanced with the increase of TA@CeO_2 content. These results confirmed an excellent antibacterial activity of TA and CeO_2.

In vitro cell viability and proliferation

The biocompatibility and biosecurity are necessary for wound treatment in clinical applications. First, the cytotoxicity and cell proliferation of CeO_2 and TA@CeO_2 particles against fibroblasts (L929 cells) were evaluated by CCK-8 assay. Although some previous literatures have already proved that CeO_2 can promote cell proliferation and migration [16], the cytotoxicity of CeO_2 is dose-dependent. As shown in Figures 5A, it can be seen that, for CeO_2 treated cells, the cell viabilities reflecting by the optical density (OD) values were similar with that of untreated cells at the CeO_2 concentrations from 0.05 to 0.5 mg/mL.While, 1 mg/mL CeO_2 suspension expressed obvious cytotoxicity (Figure 5A), consistenting with previous report [16]. However, for TA@CeO_2 at concentrations as high as 2 mg/mL, still no cytotoxicity against L929 was detected, and the cell viabilities of L929 treated with 2 mg/mL TA@CeO_2 at day 1, 3, and 5 were all significantly higher than that of control. These results fully indicated the introduction of TA onto CeO_2 could greatly reduce the cytotoxicity of high-dose CeO_2, thus improved the superior limit value of CeO_2 when applied in wound healing. Therefore, we choose TA@CeO_2 to be loaded into CS cryogels, and the cell proliferation profile of which is shown in Figure 5C. It can be seen that from Figure 5C, CS-TA@CeO_2 cryogels significantly promoted cell proliferation. In addition, Dead/Live staining was performed and the results are shown in Figure 5D. Figure 5D revealed that a majority of cells for all groups were stained green (live cells) and remained healthy at all time points, and almost no cells were stained red (dead cells). Besides, compared to CS cryogels group, the cell amount significantly increased for CS-TA@CeO_2 cryogels. Taken together, these results indicated that the prepared CS-TA@CeO_2 cryogels exhibited excellent biocompatibility, suitable for wound dressing.

Hemostatic characterization *in vivo*

As the first step of wound healing process, hemostasis, which can prevent blood loss and avoid aggravation of injury, plays a key role in wound healing [50]. *In vivo* hemostatic capacity of CS and CS-TA@CeO_2 cryogels was evaluated by testing the hemostatic time and the amount of blood loss in a rat tail-amputation model. As shown in Figure 6A, the amount of blood loss for CS-TA@CeO_2 cryogels was significantly lower than gauze and control groups ($p < 0.01$). From Figure 6B, it can be seen that the hemostatic time was reduced from higher than 200 s for the control and gauze groups, to 185.0 ± 4.0, 106.3 ± 4.7, and 83.0 ± 3.6 s for CS, CS-TA@CeO_2-10% and CS-TA@CeO_2-15% cryogels, respectively. In addition, the amount of blood loss was reduced from 0.633 ± 0.012 and 0.483 ± 0.025 g for the control and gauze groups to 0.45 ± 0.022, 0.243 ± 0.012, and 0.127 ± 0.015 g for CS, CS-TA@CeO_2-10% and CS-TA@CeO_2-15% cryogels, respectively (Figure 6C). These results demonstrated that CS-TA@CeO_2 cryogels have favorable hemostatic ability, further facilitating their application as wound dressing.

Evaluation of wound healing *in vivo*

Wound closure

The wound healing performence of CS-TA@CeO_2 cryogels . From Figure 7A, it can be seen that the wound area of the four groups all gradually decreased over time. The wounds treated with CS-TA@CeO_2-10% and CS-TA@CeO_2-15% cryogels healed significantly faster compared to the control and CS groups, especially after day 7. At the 14^{th} day, the wounds treated with CS-TA@CeO_2-10% and CS-TA@CeO_2-15% cryogels were almost covered with epicortex, while the control and CS groups were not fully epithelialized. The wound healing ratios shown in Figure 8B indicated that the CS-TA@CeO_2 cryogels treated wounds contracted significantly faster than the control and CS groups during day 3 to day 21, indicating that the CS-TA@CeO_2 cryogels had a superior wound healing ability than the pure CS cryogels.

Histological examination

At pre-set timepoints, the histopathological analysis of the sliced wound tissues treated with CS and CS-TA@CeO_2 cryogels were evaluated by H & E and Masson's trichrome staining, and the results are shown in Figures 7C and 7D. At day 3, massive inflammatory cell infiltration was found in the wound sections for all groups. As shown in Figure 7C, CS-TA@CeO_2 significantly enhanced the formation of well-organized granulation tissue at the wound site at day 7. At day 14, inflammatory cells infiltration still could be observed and the wound was not fully reepithelialized in the control group, while more granulation tissues formed and the tissue became denser in CS-TA@CeO_2 groups. The Masson's trichrome staining images reflecting collagen deposition are shown in Figure 7D. Along with wound healing, the wounds underwent

a dynamic metabolism of collagen and remodeling. More collagen deposition was found in CS-TA@CeO_2 groups than in other groups at day 7, 14 and 21. As expected, CS-TA@CeO_2 groups also displayed well arranged collagen deposition with dense and aligned fibers. In the control and CS groups, the collagen deposition in dermis exhibited in partial incompact and hypogenetic collagen fibers. Quantitative analysis (Figure 7E) demonstrated that the collagen densities in CS-TA@CeO_2-10% (76.67 ± 2.31%) and CS-TA@CeO_2-15% (76.67 ± 2.31%) groups were much higher than that in control (56.20 ± 2.69%) and CS (71.90± 3.40%) groups. High and aligned collagen deposition is essential for preferable wound healing efficacy. These results indicated that CS-TA@CeO_2 cryogels can promote collagen deposition thus further accelerate wound healing.

Immunohistochemistry staining and real-time quantitative PCR (RT-qPCR) of inflammatory and neovascularization factors

Overdose inflammatory response may lead to further tissue damage and delayed wound healing [41]. Therefore, the two typical inflammatory factors, including TNF-α (pro-inflammatory) and IL-10 (anti-inflammatory), were estimated via immunohistochemistry staining and RT-PCR, to study the effect of CS-TA@CeO_2 cryogels in extenuating the inflammation during wound healing. As shown in Figures 8A and 8B, acute TNF-α positive cells or pro-inflammatory cells infiltration, espacially on the wounded tissue sites, was found for the control and CS groups at day 3 and 7. While, the densities of TNF-α positive cells significantly reduced for CS-TA@CeO_2-10% and CS-TA@CeO_2-15% groups. This phenomenon was also confirmed by the TNF-α expression in mRNA level shown in the Figure 8G. The decay of inflammatory reponse for all groups along with time was also reflected in both the TNF-α staining images (Figure 8A), the quantitive analysis results of TNF-α positive cells (Figure 8B), as well as the TNF-α expression in mRNA level (Figure 8G), but the inflammatory reponse decay rates of CS-TA@CeO_2 groups was much faster than that of the control and CS groups. On the contrary, From Figures 8C and 8D, it can be seen that at day 3 days, there was almost no expression of IL-10 in the control and CS groups, while a small amount of IL-10 expression was found in CS-TA@CeO_2-10% and CS-TA@CeO_2-15% groups, which was also further confirmed by the RT-PCR results shown in Figure 8H. From day 3 to day 14, the expression of IL-10 gradually increased. Specially, at day 14, a large amount of IL-10 was expressed in CS-TA@CeO_2-10% and CS-TA@CeO_2-15% groups, while only a little amount of IL-10 expression could be found in the control and CS groups. All the results demonstrating that CS-TA@CeO_2 cryogels can effectively inhibit inflammatory responses and accelerate the wound healing process by promoting anti-inflammatory cytokines expression and inhibiting anti-inflammatory cytokines expression.

In addition, the neovascularization of the wounds was evaluated by immunostaining staining of CD31 (an endothelial cell marker) 3, 7, 14 and 21 days after treatment. As shown in Figures 8E and 8F, CS and CS-TA@CeO_2 cryogels treated groups displayed significantly improved CD31 expression, compared to the

control group, indicating the formation of more capillaries with mature structures in CS and CS-TA@CeO_2 groups. This was further confirmed in mRNA level as shown in the RT-PCR results of CD31 (Figure 8I). A significant increase of CD31 expression was observed in CS-TA@CeO_2-10% and CS-TA@CeO_2-15% groups, while the expression of CD31 was little in other groups. These results suggested that TA@CeO_2 loading can improve angiogenesis and promote wound healing. At day 3, 7 and 14, the expression of CD31 in mRNA level increased much faster for CS-TA@CeO_2-15% group than other groups (Figure 8I). Interestingly, as shown in Figure 8I, at day 21, the expression of CD31 decreased, this might impyed a return of CD31 expression to normal levelsand the wound healing process almost completed.

Materials And Methods

Materials

$Ce(NO_3)_3{\cdot}6H_2O$ (98%), 2,2-diphenyl-1-picrylhydrazyl (DPPH, 96%), sodium acetate (CH_3COONa, AR, 99%) and tannic acid (TA, M_w = 1701.2 Da) were purchased from Shanghai Macklin Biochemical Co., Ltd.. Acetic acid (CH_3COOH, AR) and ethanol were provided by the Guangzhou Chemical Reagent Plant. Dulbecco's modified Eagle's medium (DMEM), fetal bovine serum (FBS), trypsin, penicillin/streptomycin (PS) were obtained from Gibco Company (Grand Island, NY, USA). The Cell Counting Kit-8 (CCK-8) was purchased from Nanjing Jiancheng Bioengineering Institute. The Live/Dead Cell Staining kit (acridine orange/ethidium bromide (AO/EB), Solarbio, China) was purchased from Beijing Solarbio Science & Technology Co., Ltd. All chemical reagents were of analytical grade and used without further purification.

Synthesis of CeO_2 and TA@CeO_2 microcubes

CeO_2 microcubes was synthesized via a facile hydrothermal method. Briefly, 2.17 g $Ce(NO_3)_3{\cdot}6H_2O$ was dissolved in a mixture solution (~100 mL) containing 10 g CH_3COONa, 10 mL CH_3COOH and 60 mL water. After being dissolved completely, the solution was then transferred into a 100 mL Teflon-lined stainless steel autoclave and heated to 150 °C for 24 hours. After cooling to room temperature, the product was collected, centrifuged and washed with deionized water and ethanol for several times, and freeze-dried for further characterizations.

For the synthesis of TA coated CeO_2 (TA@CeO_2) microcubes, 1 g TA power was dissolved in 10 mL deionized water with vigorous stirring. Then, 1 g CeO_2 microcubes was dispersed in TA solution and stirred at room temperature for 12 hours. Subsequently, the crude product was centrifuged and washed with deionized water and ethanol for several times. After being freeze-dried, purified TA@CeO_2 microcubes was obtained.

Synthesis of CS-TA@CeO_2 cryogels

Chitosan (CS) solution was prepared by dissolving CS powder in a 2% (v/v) acetic acid aqueous solution. A certain amount of TA@CeO_2 (5, 10, and 15 wt% to CS) was dispersed in 1 mL deionized water and the mixture was sonicated for 20 minutes, until a homogenous suspension was obtained. After that, TA@CeO_2 solutions were gradually added to CS solution, and stirred magnetically for 2 hours at room temperature. Then, the CS or CS-TA@CeO_2 solution was added into the wells of 24-well plates with 1 mL/well, the plates were then frozed at -20 °C. After freeze-drying, the cryogels were further washed with 2 wt% NaOH solution and distilled water to remove excessive acid, and freeze-dried again. The CS, CS-TA@CeO_2-5%, CS-TA@CeO_2-10% and CS-TA@CeO_2-15% cryogels were obtained.

Characterizations

The morphology of the relevant samples was observed by scanning electron microscopy (SEM, XL30 FESEM FEG, PHILIPS) at an acceleration voltage of 20 kV.

The crystalline phases of the relevant samples were examined by X-ray diffractometer (XRD, MiniFlex-600, Rigaku Corporation, Japan) using Cu-Kα radiation at 40 kV voltage and 40 mA current. And the spectra were recorded at a 2θ from 10° to 90° with a scan rate of 10 °/min.

Thermogravimetry analysis (TGA) was carried out with a thermogravimetric analyzer (209F3-ASC, Germany, Netzsch). The relevant samples were heated from room temperature to 800 °C at a heating rate of 10 °C/min under N_2 atmosphere.

Porosity and swelling ratio tests

The porosities of CS and CS-TA@CeO_2 cryogels were determined using an alcohol immersion method described in previous literature [51]. Typically, CS and CS-TA@CeO_2 cryogels were weighted (W_1) and immersed in ethanol until saturated (the total weight was recorded as W_2). The porosity was calculated using the following equation:

$$\text{Porosity}\ (\%) = \frac{W_2 - W_1}{\rho V} \times 100\%$$

where V is the volume of the sample and ρ is the density of ethanol. Three parallel experiments were carried out for each specimen and the results were averaged.

The swelling performance of CS and CS-TA@CeO_2 cryogels was evaluated by gravimetric method [11]. Briefly, the samples were weighted (W_1) and placed in deionized water at 37 °C for 2 hours. After that, the samples were blotted with a filter paper to absorb surface excess deionized water and weighted (W_2).

Three parallel experiments were carried out and the swelling ratio was calculated using the following equation:

$$\text{Swelling}\ (\%) = \frac{W_2 - W_1}{W_1} \times 100\%$$

Antioxidant activity assay

The antioxidant efficiency of CS and CS-TA@CeO_2 cryogels was evaluated by the method of scavenging the stable 1, 1-diphenyl-2-picrylhydrazyl (DPPH) free radical. [1] DPPH was dispersed in methanol with a concentration of 0.1 mM. Then, 5 mg CS-TA@CeO_2 cryogels was added into 3 mL DPPH solution and incubated in a dark place for 30 minutes. After that, wavelength scanning was performed using UV-vis spectrophotometer (SHIMADZU UV-2550) at pre-set time-points. The absorbance at 516 nm was measured and used to calculate the DPPH degradation using the following equation [52]:

$$\text{DPPH scavenging}\ (\%) = \frac{A_B - A_S}{A_B} \times 100\%$$

where A_B, A_S were the absorption of the blank (DPPH + methanol) and the absorption of the tested specimen (DPPH + methanol + specimen), respectively.

Antibacterial studies

The antibacterial performance of the CS and CS-TA@CeO_2 cryogels was evaluated using *S. aureus* (ATCC 25923) and *E. coli* (ATCC 25922) as Gram-positive and Gram-negative bacteria, respectively. Firstly, the bacteria suspensions (10^6 CFU mL^{-1}) were spread on the solidified agar gel in Petri dish for inoculation. Then, the CS, CS-TA@CeO_2-5% and CS-TA@CeO_2-10% cryogels were placed on top of agar plates, respectively. After being cultured for 16 hours at 37 °C, the inhibition zone diameters were measured to assess the inhibition effect of the samples against the tested bacterium.

To further investigate the antibacterial ability of the CS-TA@CeO_2 cryogels, 50 mg sterilized samples were put into 10 mL of sterilized PBS (pH 7.4) solution containing 200 μL bacterial suspension (10^6 CFU mL^{-1}), and the mixture was incubated at 37 °C under stirring at 150 rpm. At pre-set time points, the suspension was collected and diluted, and the optical density (OD) was recorded by a micro-reader at 570 nm.

Cell proliferation and viability

Mouse fibroblast cells (L929) were cultured in Dulbecco's modified Eagle's medium (DMEM) supplemented with 10% fetal bovine serum (FBS) and 1% penicillin/streptomycin at 37 °C with 5% CO_2 in a humidified incubator (Thermo Fisher Scientific, USA).

The proliferation of L929 cells was evaluated using CCK-8. Briefly, CS and CS-TA@CeO_2 cryogels were sterilized by soaking in 75% ethanol followed by UV-irradiation for another 4 hours. Then, the samples were washed with sterile PBS (pH 7.4) and cell culture medium, and put into 24-well tissue culture polystyrene plates (TCPs, Costar, USA). After that, L929 cells were seeded in 24-well plates with a cell density of 1×10^4 cells/well, and incubated for 1, 3 and 5 days. At pre-determined time-points, the absorbance at 450 nm was recorded using a plate-reader after the cells were incubated with CCK-8 for 1 hour. Five parallel wells were set for each sample and the results were averaged.

The cell morphology and activity were also evaluated by Live/Dead assay according to the manufacturer's instruction. Typically, the cells were cultured for pre-set periods, and incubated with Live/Dead staining media for 10 minutes. Then, the stained cells were observed under an inversed fluorescent microscope (Olympus CKX41, Tokyo, Japan) after washing with sterile PBS (pH 7.4).

In vivo evaluation

Hemostatic evaluation experiments

The *in vivo* hemostatic ability of CS-TA@CeO_2 cryogels were evaluated using the rat tail amputation model [3, 24]. Typically, fifteen male Sprague-Dawley (SD) rats with a weight of 230-250 g were randomly divided into five groups equally, which were treated with gauze, CS, CS-TA@CeO_2-5%, CS-TA@CeO_2-10% respectively. And a negative control without any treatment was also set. Before the experiment, SD rats were anesthetized with sodium pentobarbital and the tails were cut at the 30% length of tail to the end, followed by exposing the tail in air for 15 s. After that, gauze, different treatments were applied to evaluate the hemostatic performance by recording the weight of blood loss and the hemostatic time.

Animal model

To evaluate the wound healing performance of CS-TA@CeO_2 cryogels, twelve male Sprague-Dawley (SD) rats (240-280 g) were used for the full-thickness skin wound healing experiments. All animal experiments were conducted in compliance with the Animal Experimental Committee of Southern Medical University (Approval No. SYXK2016-0167). After anesthetization, four wounds with a diameter of 1.2 cm were created on the back of each rat. After that, the wounds were covered with CS, CS-TA@CeO_2-5% and CS-TA@CeO_2-10% cryogels respectively, and PBS treatment group was also set as control. After pre-set time points, the macroscopic photographs of the treated wounds were recorded. The wound sizes were

measured by an Image J software, and the wound closure ratios were also calculated using the following equation [53].

$$\text{Wound closure ratio (\%)} = \frac{(A_0 - A_t)}{A_0} \times 100\%$$

where A_0 and A_t are the initial wound area and wound area at indicated time of “t”, respectively.

Histology and immunohistochemistry evaluation

For histological examination, the harvested wound tissues at pre-determined time-points were fixed with 4% paraformaldehyde and embedded in paraffin, and sliced into 4 μm to prepare the pathological slides. After that, hematoxylin and eosin (H & E) and Masson’s trichrome staining of the sliced tissue sections were conducted to analyze the microscopic wound regeneration in different phases. Immunohistochemical staining of TNF-α and IL-10 were performed to evaluate the inflammatory reaction in granulation tissues. Similarly, immunohistochemical staining of CD31 was also conducted followed a standard protocol to assess the angiogenesis.

Real-time quantitative PCR (RT-qPCR) analysis

The expression of inflammatory and angiogenic related genes (tumor necrosis factor-α (TNF-α), interleukin-10 (IL-10) and platelet endothelial cell adhesion molecule-1 (CD31)) by wounded tissue after being treated with different samples was analyzed by real-time quantitative PCR (RT-qPCR) assay. The total RNA was isolated from granulated tissue for complementary DNA (cDNA) synthesis. Finally, RT-qPCR (iQSYBR Green Supermix Detection System, Bio-Rad) analysis was performed with a house keeping gene GAPDH on Light Cycler 480 SYBR green (Roche) and analyzed using Q-PCR instrument (Bio-Rad, USA).

Determination of antioxidant enzyme activities

The oxidative stress markers, including activities of catalase (CAT) and superoxide dismutase (SOD) in rats wound tissue homogenate were determined using the assay kits (SOD CAT, CUSABIO Co, Wuhan, China), according to the manufacturer's instruction.

Statistical analysis

Statistical analysis was performed using one-tailed Student’s t-test by Statistical software (SPSS). The experimental results were expressed as mean ± standard deviation (SD). The differences were considered

statistically significant when the p-values were < 0.05. * and ** represent $p < 0.05$ and $p < 0.01$, respectively.

Conclusions

Excessive reactive oxygen species (ROS), strong inflammatory response, and bacterial infections would make the wound sites vulnerable and greatly slow down wound healing process. To address these problems, a highly effective and well-known rare earth-based ROS scavenger, ceria (cerium oxide, CeO_2), was firstly modified with tannic acid (TA) to give TA coated CeO_2 (TA@CeO_2) microcubes, which was further introduced into chitosan (CS) to fabricate TA-bridged CeO_2 microcubes and CS cryogels (CS-TA@CeO_2) through hydrogen bonding interactions between TA and CS. Benefit from the highly interconnected and porous structure (porosity > 80%), the CS-TA@CeO_2 cryogels could absorb the excessive wound exudate and provide a moist environment for wound healing. The CS-TA@CeO_2 cryogels exhibited excellent antioxidant ability evidenced by scavenging more than 82.9% ROS *in vitro* and significantly increasing the antioxidant enzyme levels *in vivo*. The anti-inflammatory ability of the cryogels was also confirmed by the downregulated expression of the inflammatory cytokine, TNF-α and the upregulated expression of the anti-inflammatory cytokine, IL-10. The CS-TA@CeO_2 cryogels can promote the adhesion and proliferation of mouse fibroblasts (L929) cells. In addition, the CS-TA@CeO_2 cryogels showed excellent antibacterial, hemostatic and angiogenic activities. The *in vivo* full-thickness skin wound healing experiments on Sprague-Dawley (SD) rats demonstrated that the multifunctional CS-TA@CeO_2 cryogels can significantly accelerate wound healing through providing considerable antioxidant activity, promoting angiogenesis, and increasing collagen deposition. The developed multifunctional CS-TA@CeO_2 cryogels hold a great potential in clinical applications as wound dressing to promote wound healing, espacially when excessive ROS, inflammatory response, or bacterial infection was involved. The development strategy of CS-TA@CeO_2 cryogels could also be expanded to other organic/inorganic composite material designs for more broad biomedical applications such as wound healing and bone regeneration.

Declarations

Acknowledgements

Not applicable.

Authors' contributions

MZT: Performed the animal experiments, Date curation, Writing-Original draft. ZJL: Performed the in vitro assays, Helped to conduct the in vivo animal experiments, Writing-Original draft. ZHL: Helped to perform the in vitro assays, Project administration. Funding acquisition. KKW: Proposed research ideas and

design research schemes, Synthesized and characterized properties of the materials, Project administration, Funding acquisition, Directed the whole article. JSG: Proposed research ideas and design research schemes, Directed the whole article. All authors read and approved the final manuscript.

Funding

This work was supported by a Natural Science Foundation of China (82102545) and a Joint Foundation for Basic and Applied Basic Research Project of Guangdong Province (Grant No. 2020A1515110062).

Availability of data and materials

The datasets supporting the conclusions of this article are included within the article, also can be obtained from the corresponding author on reasonable request.

Ethics approval and consent to participate

All animal experiments were conducted in compliance with the Animal Experimental Committee of Southern Medical University (Approval No. SYXK2016-0167).

Consent for publication

All authors read and approved the fnal manuscript for publication

Competing interests

The authors declare no conflict of interest.

Author details

1 Department of Histology and Embryology, School of Basic Medical Sciences, Guangdong Provincial Key Laboratory of Bone and Joint Degeneration Diseases, The Third Affiliated Hospital of Southern Medical University, Southern Medical University, Guangzhou, 510515, China

2 The Second Clinical Medical College of Lanzhou University, Lanzhou 730030, Gansu, China; Lanzhou University Second Hospital, Lanzhou 730030, Gansu, China; Key Laboratory of Digestive System Tumors of Gansu Province, Lanzhou 730030, Gansu, China

3 Molecular Diagnosis and Treatment Center for Infectious Diseases, Dermatology Hospital, Southern Medical University, Guangzhou 510091, China.

References

1. Wu K, Wu X, Chen M, Wu H, Jiao Y, Zhou C. H_2O_2-responsive smart dressing for visible H_2O_2 monitoring and accelerating wound healing. Chem. Eng. J. 2020; 387: 124127.
2. Liang Y, Li Z, Huang Y, Yu R, Guo B. Dual-dynamic-bond cross-linked antibacterial adhesive hydrogel sealants with on-demand removability for post-wound-closure and infected wound healing. ACS Nano, 2021; 15(4): 7078–93.
3. Yu Y, Li P, Zhu C, Ning N, Zhang S, Vancso GJ. Multifunctional and recyclable photothermally responsive cryogels as efficient platforms for wound healing. Adv. Funct. Mater. 2019; 29(35): 1904402.
4. Huang W, Ying R, Wang W, Guo Y, He Y, Mo X, et al. A macroporous hydrogel dressing with enhanced antibacterial and anti-inflammatory capabilities for accelerated wound healing. Adv. Funct. Mater. 2020; 30(21): 2000644.
5. Haghniaz R, Rabbani A, Vajhadin F, Khan T, Kousar R, Khan AR, et al. Anti-bacterial and wound healing-promoting effects of zinc ferrite nanoparticles. J. Nanobiotechnol. 2021; 19(1): 1–15.
6. Zhao H, Huang J, Li Y, Lv X, Zhou H, Wang H, et al. ROS-scavenging hydrogel to promote healing of bacteria infected diabetic wounds. Biomaterials. 2020; 258: 120286.
7. Feng X, Xu W, Li Z, Song W, Ding J, Chen X. Disease Immunotherapy: immunomodulatory nanosystems. Adv. Sci. 2019; 6(17): 1970100.
8. Saleh B, Dhaliwal HK, Portillo-Lara R, Shirzaei Sani E, Abdi R, Amiji MM, et al. Local immunomodulation using an adhesive hydrogel loaded with miRNA-laden nanoparticles promotes wound healing. Small. 2019; 15(36): 1902232.
9. Hou S, Y Liu, F Feng, J Zhou, Feng X, Fan Y. Polysaccharide-peptide cryogels for multidrug-resistant-bacteria infected wound healing and hemostasis. Adv. Healthc. Mater. 2020; 9(3): 1901041.
10. Yao L, Gao H, Lin Z, Dai Q, Zhu S, Li S, et al. A shape memory and antibacterial cryogel with rapid hemostasis for noncompressible hemorrhage and wound healing. Chem. Eng. J. 2022; 428: 131005.
11. Xia G, Zhai D, Sun Y, Hou L, Guo X, Wang L, et al. Preparation of a novel asymmetric wettable chitosan-based sponge and its role in promoting chronic wound healing. Carbohyd. Polym. 2020; 227: 115296.
12. Chi J, Zhang X, Chen C, Shao C, Zhao Y, Wang Y. Antibacterial and angiogenic chitosan microneedle array patch for promoting wound healing. Bioact. Mater. 2020; 5(2): 253–59.
13. Soubhagya AS, Moorthi A, Prabaharan M. Preparation and characterization of chitosan/pectin/ZnO porous films for wound healing. Int. J. Biol. Macromol. 2020; 157: 135–45.
14. Liu Y, Xiao Y, Cao Y, Guo Z, Li F, Wang L. Construction of Chitosan-Based Hydrogel Incorporated with Antimonene Nanosheets for Rapid Capture and Elimination of Bacteria. Adv. Funct. Mater. 2020; 30(35): 2003196.
15. Zheng H, Wang S, Cheng F, He X, Liu Z, Wang W, et al. Bioactive anti-inflammatory, antibacterial, conductive multifunctional scaffold based on MXene@CeO_2 nanocomposites for infection-impaired

skin multimodal therapy. Chem. Eng. J. 2021; 424: 130148.

16. Ma T, Zhai X, Huang Y, Zhang M, Zhao X, Du Y, et al. A Smart Nanoplatform with Photothermal Antibacterial Capability and Antioxidant Activity for Chronic Wound Healing. Adv. Healthc. Mater. 2021; 10: 2100033.
17. Augustine R, Zahid AA, Hasan A, Dalvi YB, Jacob J. Cerium oxide nanoparticle-loaded gelatin methacryloyl hydrogel wound-healing patch with free radical scavenging activity. ACS Biomater. Sci. Eng. 2020; 7(1): 279–90.
18. Kim DW, Le TMD, Lee SM, Kim HJ, Ko YJ, Jeong JH, et al Microporous organic nanoparticles anchoring CeO_2 materials: reduced toxicity and efficient reactive oxygen species-scavenging for regenerative wound healing. ChemNanoMat, 2020; 6(7): 1104–10.
19. Zhuo M, Ma J, Quan X. Cytotoxicity of functionalized CeO_2 nanoparticles towards Escherichia coli and adaptive response of membrane properties. Chemosphere, 2021, 281: 130865.
20. Zabihi E, Arab-Bafrani Z, Hoseini SM, Mousavi E, Babaei A, Khalili M, et al. Fabrication of nano-decorated ZnO-fibrillar chitosan exhibiting a superior performance as a promising replacement for conventional ZnO. Carbohyd. Polym. 2021; 274: 118639.
21. Fiandra L, Bonfanti P, Piunno Y, Nagvenkar AP, Perlesthein I, Gedanken A, et al. Hazard assessment of polymer-capped CuO and ZnO nanocolloids: A contribution to the safe-by-design implementation of biocidal agents. NanoImpact, 2020; 17: 100195.
22. Kim I, Viswanathan K, Kasi G, Sadeghi K, Thanakkasaranee S, Seo J. Poly (lactic acid)/ZnO bionanocomposite films with positively charged ZnO as potential antimicrobial food packaging materials. Polymers, 2019; 11(9): 1427.
23. Khan MI, Paul P, Behera SK, Jena B, Tripathy SK, Lundborg CS, et al. To decipher the antibacterial mechanism and promotion of wound healing activity by hydrogels embedded with biogenic Ag@ZnO core-shell nanocomposites. Chem. Eng. J. 2021; 417: 128025.
24. Li L, Yang Z, Fan W, He L, Cui C, Zou J, et al. In situ polymerized hollow mesoporous organosilica biocatalysis nanoreactor for enhancing ROS-mediated anticancer therapy. Adv. Funct. Mater, 2020; 30(4): 1907716.
25. Ejima H, Richardson JJ, Liang K, Best J, Koeverden MP, Such GK, et al. One-step assembly of coordination complexes for versatile film and particle engineering. Science, 2013; 341(6142): 154–57.
26. Sun Y, Li X, Zhao M, Chen Y, Xu Y, Wang K, et al. Bioinspired supramolecular nanofiber hydrogel through self-assembly of biphenyl-tripeptide for tissue engineering. Bioact. Mater. 2022; 8: 396–08.
27. Peng Q, Wu Q, Chen J, Wang T, Wu M, Yang D, et al. Coacervate-based instant and repeatable underwater adhesive with anticancer and antibacterial properties. ACS Appl. Mater. Interfaces, 2021; 13(40): 48239–51.
28. Liu L, Ge C, Zhang Y, Ma W, Su X, Chen L, et al. Tannic acid-modified silver nanoparticles for enhancing anti-biofilm activities and modulating biofilm formation. Biomater. Sci. 2020; 8(17): 4852–60.

29. Guo J, Sun W, Kim JP, Lu X, Li Q, Lin M, et al. Development of tannin-inspired antimicrobial bioadhesives. Acta Biomater, 2018; 72: 35–44.
30. Guo J, Tian X, Xie D, Rahn K, Gerhard E, Kuzma ML, et al. Citrate-based tannin-bridged bone composites for lumbar fusion. Adv. Funct. Mater. 2020; 30(27): 2002438.
31. Cao C, Yang N, Zhao Y, Yang D, Hu Y, Yang D, et al. Biodegradable hydrogel with thermo-response and hemostatic effect for photothermal enhanced anti-infective therapy. Nano Today, 2021; 39: 101165.
32. Han L, Li P, Tang P, Wang X, Zhou T, Wang K, et al. Mussel-inspired cryogels for promoting wound regeneration through photobiostimulation, modulating inflammatory responses and suppressing bacterial invasion. Nanoscale, 2019; 11(34): 15846–61.
33. Zhao X, Guo B, Wu H, Liang Y, Ma P X. Injectable antibacterial conductive nanocomposite cryogels with rapid shape recovery for noncompressible hemorrhage and wound healing. Nat. Commun. 2018; 9(1): 1–17.
34. Ma M, Zhong Y, Jiang X. Thermosensitive and pH-responsive tannin-containing hydroxypropyl chitin hydrogel with long-lasting antibacterial activity for wound healing[J]. Carbohyd. Polym., 2020, 236: 116096.
35. Wu K, Wu X, Guo J, Jiao Y, Zhou C. Facile Polyphenol-europium assembly enabled functional Poly (l-Lactic Acid) nanofiber mats with enhanced antioxidation and angiogenesis for accelerated wound healing. Adv. Healthc. Mater. 2021; 10: 2100793.
36. Taheri P, Jahanmardi R, Koosha M, Abdi S. Physical, mechanical and wound healing properties of chitosan/gelatin blend films containing tannic acid and/or bacterial nanocellulose. Int. J. Biol. Macromol. 2020, 154: 421–32.
37. Wu K, Liu X, Li Z, Jiao Z, Zhou C, Fabrication of chitosan/graphene oxidecomposite aerogel microspheres with high bilirubin removal performance. *Mat. Sci. Eng. C-Mater.* 2020; *106*: 110162.
38. Fan Z, Liu B, Wang J, Zhang S, Lin Q, Gong P, et al. A novel wound dressing based on Ag/Graphene polymer hydrogel: effectively kill bacteria and accelerate wound healing. Adv. Funct. Mater. 2014; 24(25): 3933–43.
39. Lu S, Zhang X, Tang Z, Xiao H, Zhang M, Liu K, et al. Mussel-inspired blue-light-activated cellulose-based adhesive hydrogel with fast gelation, rapid haemostasis and antibacterial property for wound healing. Chem. Eng. J. 2021; 417: 129329.
40. Li M, Zhang Z, Liang Y, He J, Guo B, Multifunctional tissue-adhesive cryogel wound dressing for rapid nonpressing surface hemorrhage and wound repair. ACS Appl. Mater. Interfaces, 2020; 12(32): 35856–72.
41. Wang T, Zhou Z, Liu J, Zhou Z, Dai Y, Hou Z, et al. Donut-like MOFs of copper/nicotinic acid and composite hydrogels with superior bioactivity for rh-bFGF delivering and skin wound healing. J. Nanobiotechnol. 2021; 19(1): 1–21.
42. Mao L, Wang L, Zhang M, Ullah MW, Liu L, Zhao W, et al. In Situ Synthesized Selenium Nanoparticles-Decorated Bacterial Cellulose/Gelatin Hydrogel with Enhanced Antibacterial, Antioxidant, and Anti-

Inflammatory Capabilities for Facilitating Skin Wound Healing. Adv. Healthcare. Mater. 2021; 10: 2100402.

43. Yu H, Chen X, Cai J, Ye D, Wu Y, Fan L, et al. Novel porous three-dimensional nanofibrous scaffolds for accelerating wound healing. Chem. Eng. J. 2019; 369: 253–62.
44. Chen Y, Liang Y, Liu J, Yang J, Jia N, Zhu C, et al. Optimizing microenvironment by integrating negative pressure and exogenous electric fields via a flexible porous conductive dressing to accelerate wound healing. Biomater. Sci. 2021; 9(1): 238–51.
45. Qu J, Zhao X, Liang Y, Xu Y, Ma P X, Guo B, Degradable conductive injectable hydrogels as novel antibacterial, anti-oxidant wound dressings for wound healing. Chem. Eng. J. 2019; 362: 548–60.
46. Tao B, Lin C, Yuan Z, He Y, Chen M, Li K, et al. Near infrared light-triggered on-demand Cur release from Gel-PDA@Cur composite hydrogel for antibacterial wound healing. Chem. Eng. J. 2021; 403: 126182
47. Q. Zeng, Y. Qian, Y. Huang, F. Ding, X. Qi, J. Shen. Polydopamine nanoparticle-dotted food gum hydrogel with excellent antibacterial activity and rapid shape adaptability for accelerated bacteria-infected wound healing. Bioact. Mater. 2021; 6(9): 2647–57.
48. Lu X, Shi S, Li H, Gerhard E, Lu Z, Tan X, et al. Magnesium oxide-crosslinked low-swelling citrate-based mussel-inspired tissue adhesives. Biomaterials, 2020; 232: 119719.
49. Zou F, Jiang J, Lv F, Xia X, Ma X. Preparation of antibacterial and osteoconductive 3D-printed PLGA/Cu(I)@ZIF-8 nanocomposite scaffolds for infected bone repair. J. Nanobiotechnol. 2020; 18(1): 1–14.
50. Ahmadian Z, Correia A, Hasany M, Figueiredo P, Dobakhti F, Eskandari MR, et al. Anti-bacterial hydrogels: A Hydrogen-bonded extracellular matrix-mimicking bactericidal hydrogel with radical scavenging and hemostatic function for pH-responsive wound healing acceleration. Adv. Healthcare. Mater. 2021; 10(3): 2170009.
51. Wu K, Song X, Cui S, Li Z, Jiao Y, Zhou C, Immobilization of bovine serum albumin via mussel-inspired polydopamine coating on electrospun polyethersulfone (PES) fiber mat for effective bilirubin adsorption. Appl. Surf. Sci. 2018; 451: 45–55.
52. Qu J, Zhao X, Liang Y, Zhang T, Ma PX, Guo B. Antibacterial adhesive injectable hydrogels with rapid self-healing, extensibility and compressibility as wound dressing for joints skin wound healing. Biomaterials, 2018; 183: 185–99.
53. Liu M, Liu T, Chen X, et al. Nano-silver-incorporated biomimetic polydopamine coating on a thermoplastic polyurethane porous nanocomposite as an efficient antibacterial wound dressing. J. Nanobiotechnol. 2018; 16(1): 1–19.

Scheme

Scheme 1 is only available as a download in the Supplemental Files section.

Figures

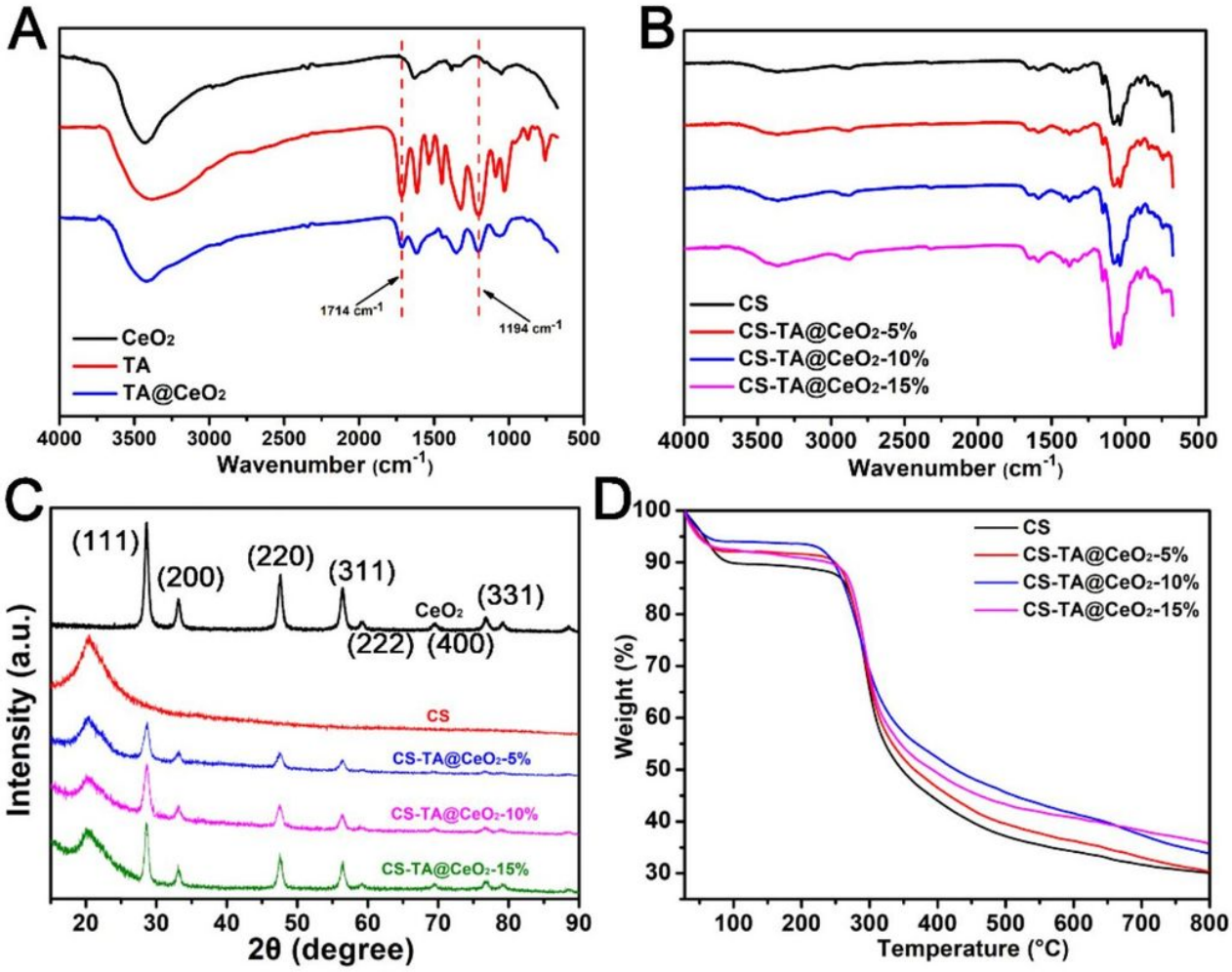

Figure 1

Characterizations of TA, CeO2, TA@CeO2, CS and CS-TA@CeO2: (A, B) FTIR spectra, (C) XRD patterns, (D) thermogravimetry analysis (TGA) curves.

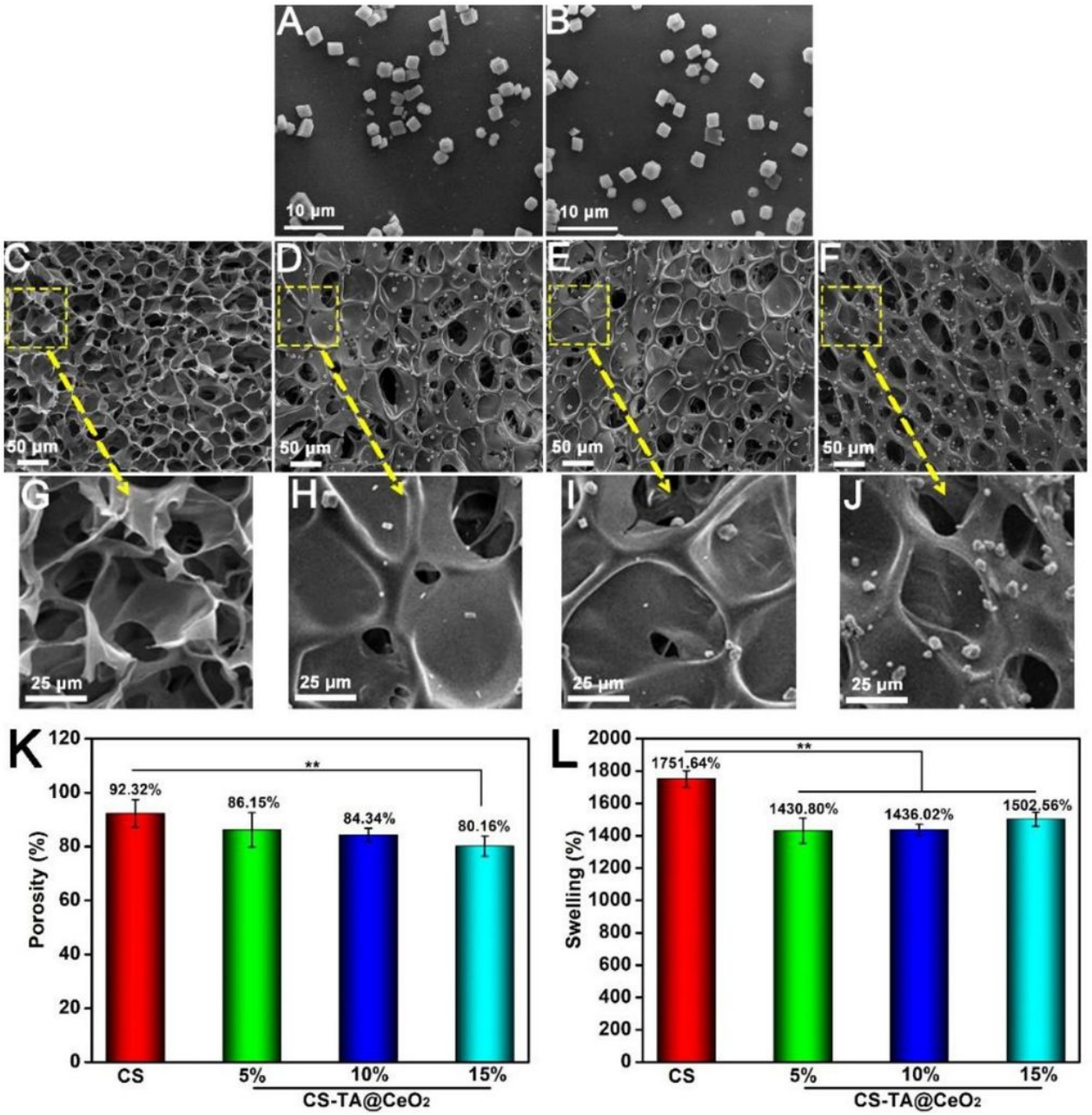

Figure 2

SEM images of (A) CeO2, and (B) TA@CeO2; (C, G) CS, (D, H) CS-TA@CeO2-5%, (E, I) CS-TA@CeO2-10% and (F, J) CS-TA@CeO2-15% cryogels; Porosities (K) and swelling ratios (L) of CS and CS-TA@CeO2 cryogels. (**p < 0.01)

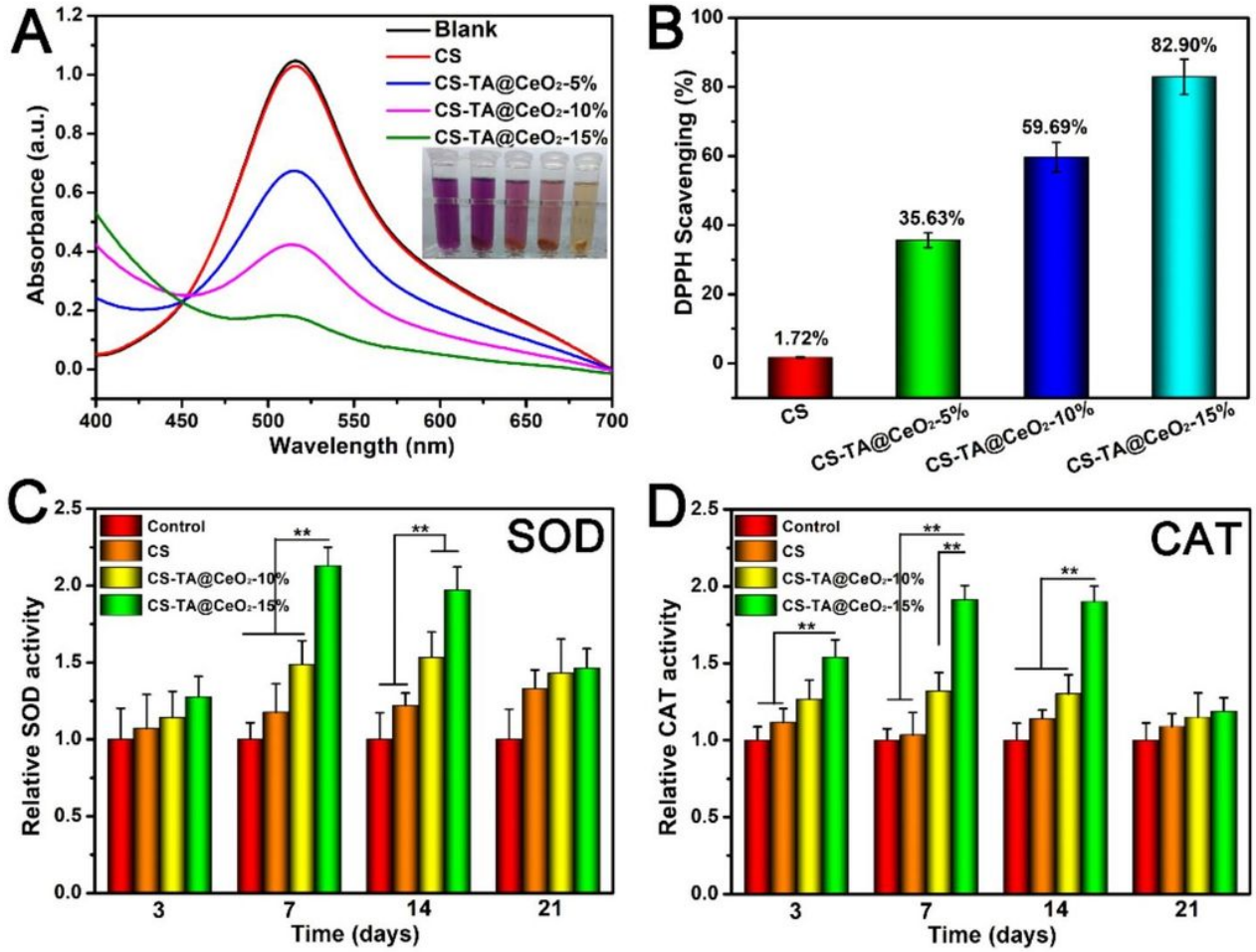

Figure 3

(A) UV-vis spectra and (B) DPPH scavenging percentages of DPPH solutions after being treated by CS and CS-TA@CeO2 cryogels for 20 minutes; Expression levels of SOD (C) and CAT (D) during the process of wound healing after the wound tissue being treated with CS and CS-TA@CeO2 cryogels for 3, 7, 14 and 21 days. (**p < 0.01)

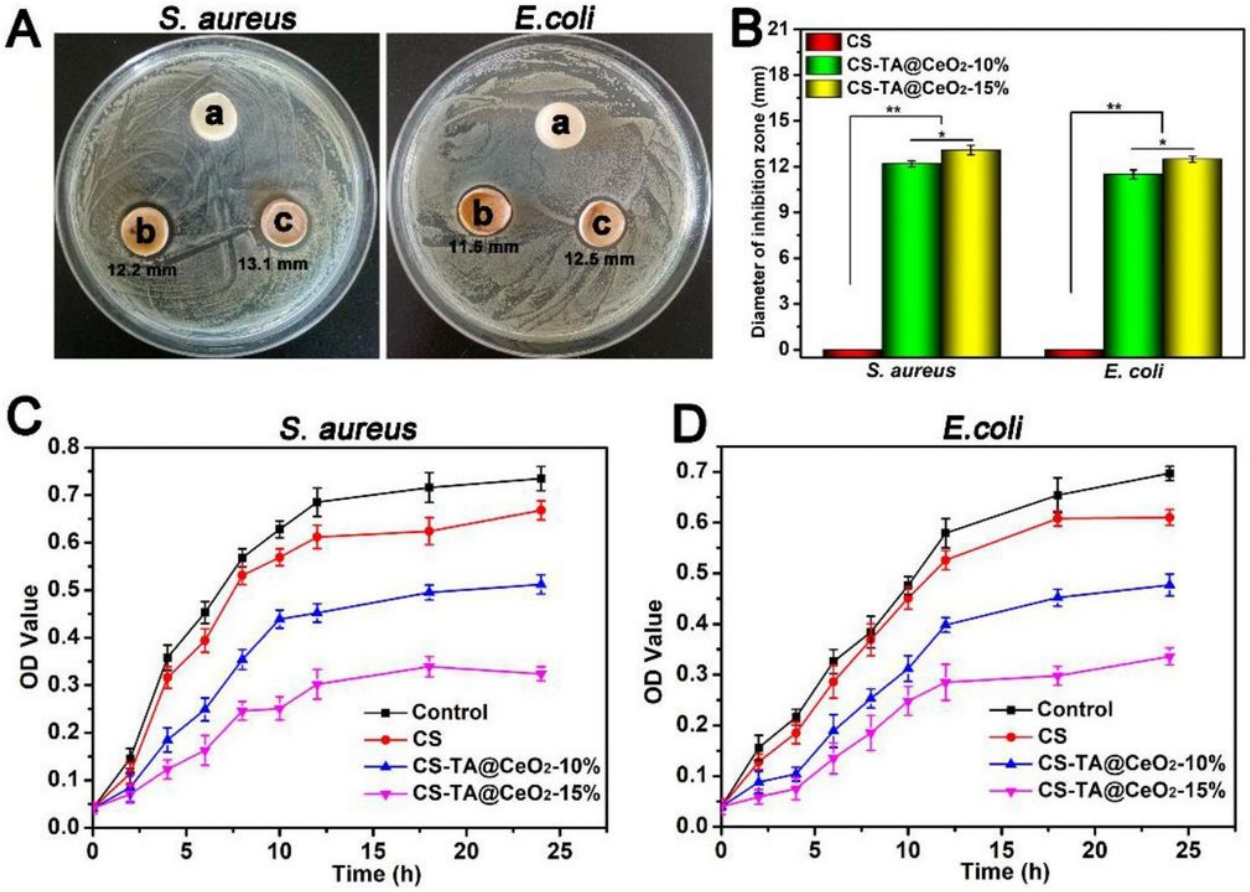

Figure 4

Antibacterial activity of CS-TA@CeO2 cryogels against S.aureus and E.coli: (A) bacterial inhibition zone images and (B) quantitative results; (C) the bacterial growth curve of S.aureus and E.coli becateria suspensions containing freeze-dried CS, CS-TA@CeO2-10% and CS-TA@CeO2-15% cryogels. (*p < 0.05, **p < 0.01)

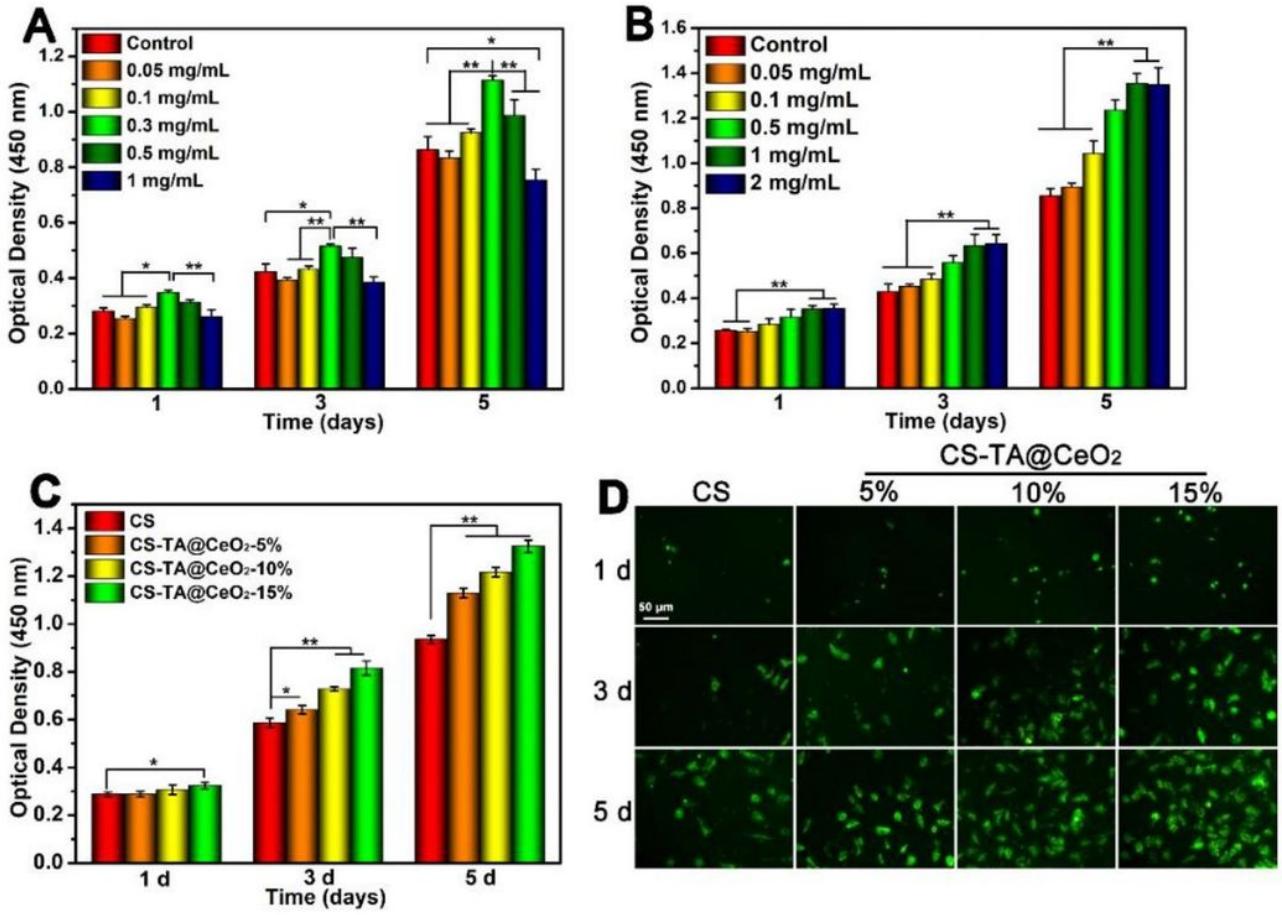

Figure 5

The cell proliferation results of L929 cells for (A) CeO2, (B) TA@CeO2, and (C) CS and CS-TA@CeO2 cryogels, tested by CCK-8 assay; (D) The Live/Dead staining images of L929 cells grown on the surface of CS and CS-TA@CeO2 cryogels for 1, 3, and 5 days. (*p < 0.05, **p < 0.01)

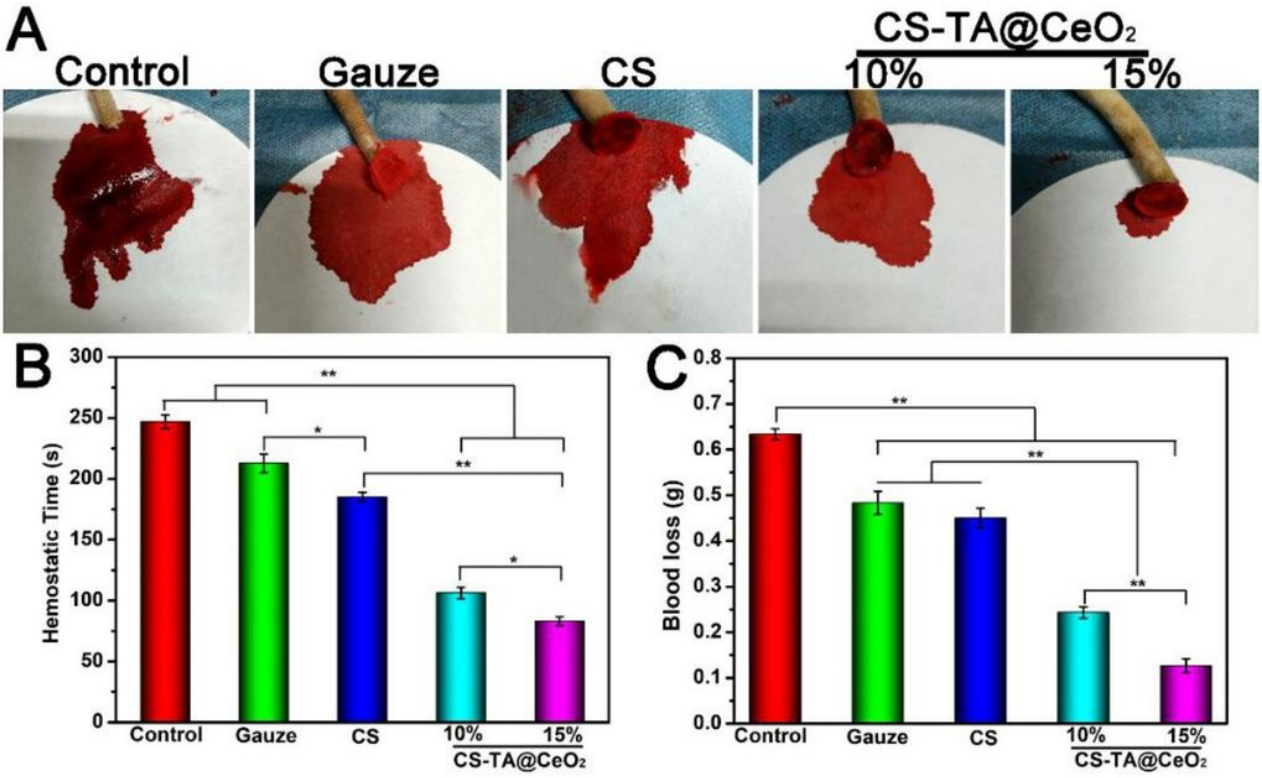

Figure 6

(A) Digital images of rat tail amputation, (B) hemostasis time and (C) blood loss weight for control (untreated), gauze, CS and CS-TA@CeO2 cryogels. (*p < 0.05, **p < 0.01)

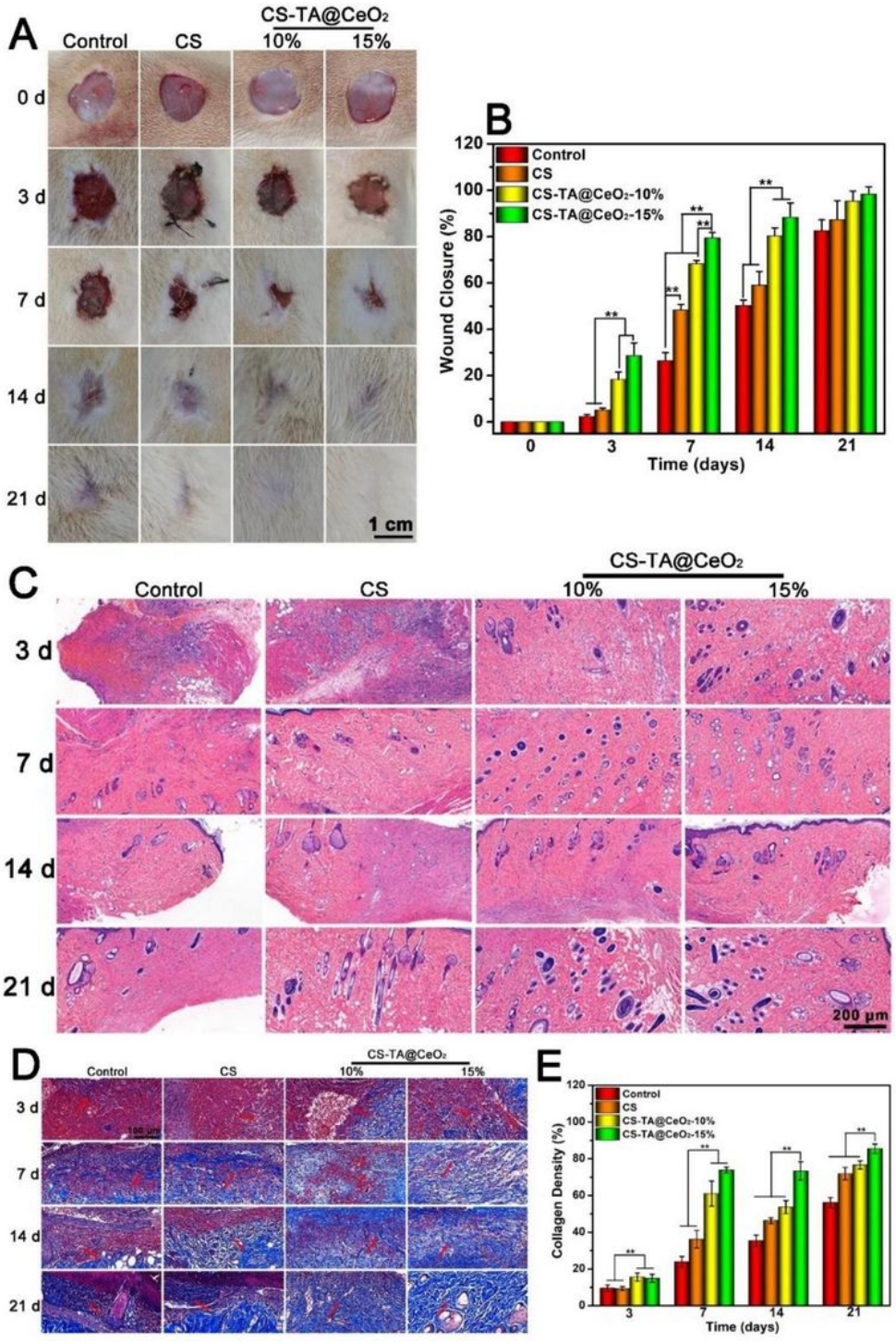

Figure 7

(A) Photographs, (B) wound closure rate, (C) H&E staining, (D) masson's trichrome staining and (E) collagen density after the created skin wounds on SD rats being treated with CS and CS-TA@CeO2 cryogels for 3, 7, 14 and 21 days. (**p < 0.01)

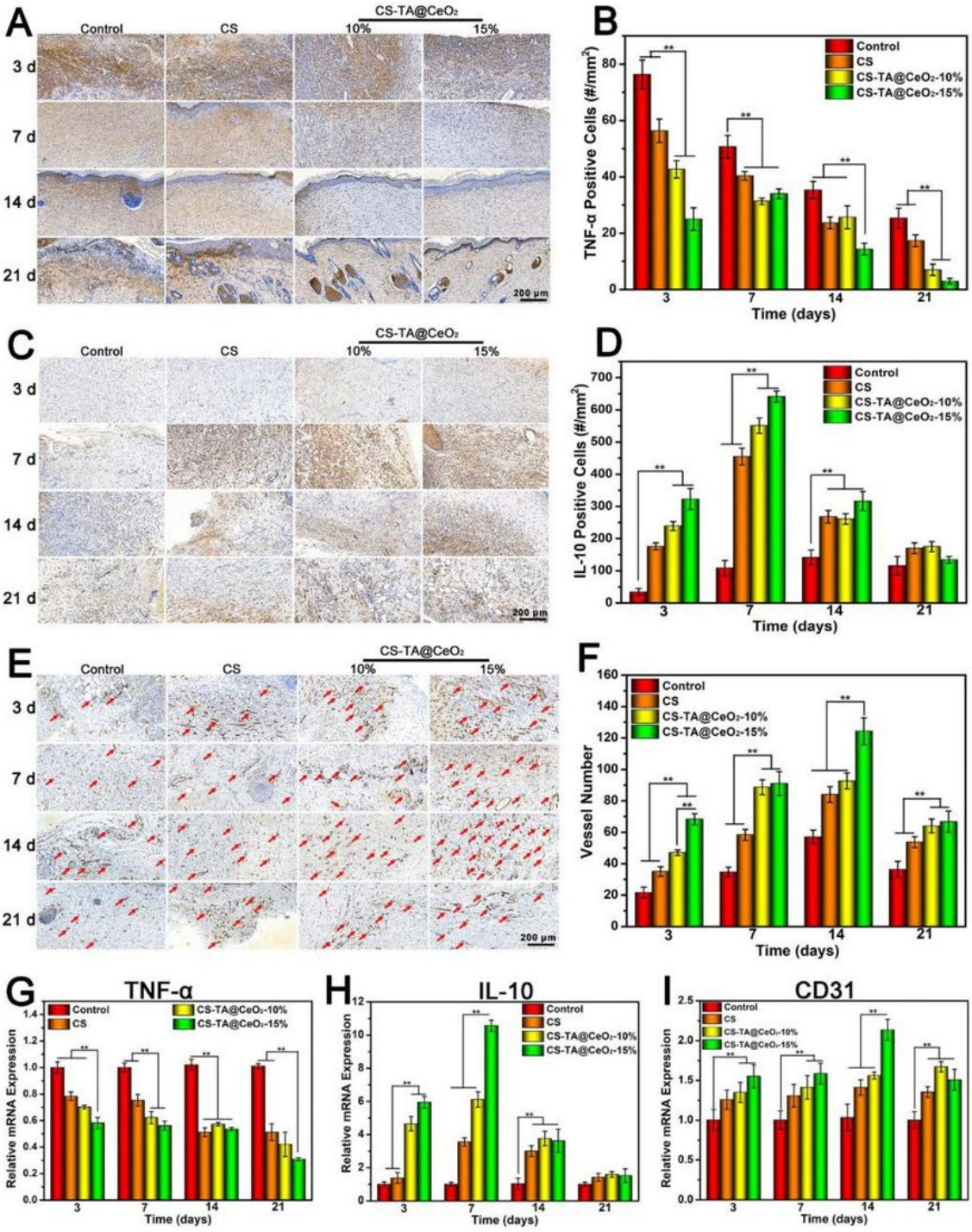

Figure 8

Immunohistochemistry staining images of (A) IL-10, (C) TNF-α and (E) CD31; quantitative (B) IL-10 and (D) TNF-α and (F) neovascularization densities after the created wound on SD rats being treated with CS and CS-TA@CeO2 cryogels for 3, 7, 14 and 21 days. (**p < 0.01; red arrows represent new blood vessels).

Supplementary Files

This is a list of supplementary files associated with this preprint. Click to download.

- Scheme1.jpg
- COT.jpg